Fabrication of Au/TiO2 nanowires@carbon fiber paper ternary composite for visible-light photocatalytic degradation of gaseous styrene

Jiayuan Shi[a], Jiangyao Chen[b], Guiying Li[b], Taicheng An[a,*], Hiromi Yamashita[c,*]

[a] State Key Laboratory of Organic Geochemistry and Guangdong Key Laboratory of Environmental Protection and Resources Utilization, Guangzhou Institute of Geochemistry, Chinese Academy of Sciences, Guangzhou 510640, China
[b] Institute of Environmental Health and Pollution Control, School of Environmental Science and Engineering, Guangdong University of Technology, Guangzhou 510006, China
[c] Division of Materials and Manufacturing Science, Graduate School of Engineering, Osaka University, 2-1 Yamadaoka, Suita, Osaka 565-0871, Japan

ARTICLE INFO

ABSTRACT

In this work, Au nanoparticles decorated TiO2 nanowires onto hierarchically porous carbon fiber paper (Au/TiO2NWs@CFP) ternary composite was synthesized using a combining approach of wet coating, hydrothermal growth and photoreduction. Characterization revealed that the 3D network of CFP was homogeneously encapsulated by Au nanoparticles (1.8 nm in diameter) decorated anatase TiO2 NWs with diameter of 15–30 nm and length of several microns. The formation of the Au/TiO2NWs@CFP composite undergoes the following three key-steps: formation of TiO2 islands on CFP, in-situ growth of TiO2 NWs on the TiO2 islands and deposition of Au NPs onto TiO2 NWs. Photocatalytic degradation of gaseous styrene showed that Au/TiO2NWs@CFP exhibited the excellent photoactivity and photostability under visible light irradiation. It is attributed to the synergistic effect of the three components (TiO2 NWs, CFP and Au nanoparticles), which can enhance visible light absorption intensity, reduce the recombination of photogenerated charges and holes, as well as improve the adsorption of organic pollutants. The present strategy would offer an effective way for the synthesis of ternary composite photocatalyst and its application to air purification under visible light irradiation.

© 2016 Elsevier B.V. All rights reserved.

1. Introduction

Heterogeneous photocatalysis of TiO2 can be initiated by UV light at room temperature and organic molecules adsorbed on the TiO2 surfaces can be oxidized to non-toxic substances such as CO2 and H2O [1,2]. However, bare TiO2 materials show poor absorption of visible light, which limits the efficient utilization of solar energy [3,4]. The fast recombination of excited electrons and holes on TiO2 also decrease its photocatalytic activity [5,6]. Therefore, various strategies have been attempted to improve the solar light photocatalytic efficiency of TiO2. Incorporation of additional components such as metals and carbonaceous materials in the TiO2 structures has been verified as one of the most promising methods [4]. Recently, the deposition of noble metal (e.g., Au, Ag, Pt) nanoparticles (NPs) on TiO2 materials also showed an enhancement

of the photocatalytic properties of the semiconductor [7,8]. Especially, coupling Au NPs with TiO2, to form Au/TiO2 nanocomposites, is considered as an efficient way to extend the spectral response of photocatalysts to the visible light region. This is due to the strong surface plasmon resonance of Au NPs derived from the collective oscillation of conductive electrons [9,10]. Under visible light irradiation, metal particles can absorb photons due to their surface plasmon resonance [11,12]. Then the excited electrons were transferred to the conduction band of TiO2, leaving the positive holes on the metal particles. With the help of those photogenerated charges, reactive oxygen species can form and be beneficial for the photocatalysis using TiO2-metal nanoparticles composite under visible light irradiation [13]. However, both TiO2 and metal nanoparticles are kinetically unstable and they tend to aggregate into larger structures, which will decrease the photocatalysis efficiency [14,15].

On the other hand, due to the unique and controllable structural as well as electrical properties, porous carbonaceous materials such as activated carbon, carbon nanotubes and fullerene become great interest for the structural support and photocatalytic enhancement of TiO2-based systems [16–18]. Firstly, these porous carbona-

ceous materials could provide high-surface area for the adsorption of organic reactants and increase active sites for photocatalysis [18–20]. Secondly, carbon structures can act as the catalyst support which is beneficial for the dispersion of TiO₂ particles [21,22]. Thirdly, the carbon species exhibiting high electrical conductivity and electron storage capacity may accept photongenerated electrons from TiO₂, thus hindering the recombination of electron-hole pairs and facilitating the reactive oxygen species formation [23]. However, the visible-light catalytic activity of carbon-TiO₂ composites is not high.

Beyond binary composite systems, multicomponent hybrid nanomaterials obtained through integrating carbon materials, noble metals and TiO₂ photocatalyst into a composite system are expected to combine the advantages of each respective component, possess multifunctional properties and show superior photocatalytic activities [24,25]. Various carbon structures, such as carbon nanotube [26], reduced graphene oxide [27] and carbon nanofiber [28] have been used for the ternary photocatalysts fabrication. However, most investigations are mainly focused on the photocatalysts in powder form, which may lead to some limitations in practical application. For instance, the agglomerated particles are willing to form, which does not favor the contact between catalysts and organics and subsequently decrease the photocatalytic efficiency. Further, powder catalysts can be easily blown away in continuous air flow systems, leading to the secondary pollution and potential threat to human health. Thus, for practical application of photocatalysis, particulate semiconductors need to be immobilized on the macroscopic materials such as nickel foam, carbon foam and graphene thin film [29,30]. Recently, carbon fibers have been made into paper which is called "carbon fiber paper (CFP)". CFP structures can be a good candidate for catalyst immobilization, which is a porous three-dimensional (3D) network of micro-sized carbon fibers with big holes and large surface area for loading of photocatalytic materials [31,32]. Therefore, the CFP-supported photocatalysis may be easy to use in application. However, no reports on preparation of the CFP-supported ternary photocatalysts with multifunctional properties for photodegradation of volatile organic compounds can be found.

In this work, Au/TiO₂NWs@CFP ternary composite photocatalyst was prepared and its physicochemical properties were characterized in details. The formation mechanism of ternary composite was investigated through time-dependent experiments and the photocatalytic activities of the catalysts were evaluated by degrading gaseous styrene under visible light irradiation. The results suggest that it is a promising approach to exploit highly efficient composite photocatalysts, which offer more opportunities for practical application of photocatalysis in environmental purification.

2. Experimental section

2.1. Materials and chemicals

Carbon fiber paper (CFP, TGP-H-60) was obtained from Toray Group, Japan. Tetrabutyltitanate (TBT) and hydrogen tetrachloroaurate (III) hydrate (HAuCl₄·3H₂O, 99.9%) were from Sigma-Aldrich, USA. NaOH and absolute ethanol were from Nanjing Chemical Reagent Co., Ltd. Degussa P25 TiO₂ was from Germany. All other reagents were analytic grade, and all aqueous solutions were prepared with deionized water.

2.2. Preparation of Au/TiO₂NWs@CFP composite

One gram of CFP constituted by carbon fibers with the diameter of 8–15 μm was first treated in a 40 mL mixture of concentrated nitric acid (65%–68%) and sulfuric acid (95%–98%) with a volume ratio of 1:3 under the temperature of 90 °C for 90 min. Then the acid-treated CFP was obtained after the sequence filtration, washing with distilled water and then drying at 80 °C.

A typical synthesis procedure for TiO₂NWs@CFP composite was as follows: 0.68 mL of TBT was dissolved into 20 mL of absolute ethanol under mild stirring. Five drops of the obtained clear solution was successively and uniformly coated onto a piece of acid-treated CFP (1 cm × 1 cm). Afterward, the wet CFP was dried in an oven at 80 °C for 30 min. These coating and drying processes were repeated for five times, and the resultant product was called "bulk TiO₂@CFP". Then, 0.4 g of P25 powder was dispersed in NaOH solution (20 mL, 5 M) with continuous stirring. The obtained suspension was hydrothermally treated in a Teflon-lined stainless-steel autoclave with a piece of bulk TiO₂@CFP at 110 °C. After 48 h, the autoclave was naturally cooled down to room temperature. The surface of CFP was found to be almost fully covered with white precipitates. The CFP was ultrasonically washed with 100 mL H₂O for 5 min, and then rinsed with distilled water until to neutral pH. After rinsing with absolute ethanol for several times, the washed CFP was dried in ambient conditions overnight. For synthesis of Au/TiO₂NWs@CFP composite, a piece of TiO₂ NWs@CFP was immersed in 50 mL of HAuCl₄·3H₂O (2.0 × 10⁻³ M) at room temperature for 3 h in the dark. Then, the mixture was irradiated with a 365 nm UV-LED spot lamp (Shenzhen Lamplic Science Co., Ltd.) for 4 h. The obtained product was washed thoroughly three times with absolute ethanol. Finally, the Au/TiO₂NWs@CFP photocatalyst was obtained after being dried at 80 °C overnight. TiO₂ NWs and Au/TiO₂ NWs were prepared with a similar procedure.

2.3. Characterization

X-ray diffraction (XRD) patterns were recorded on an Empyrean X-ray diffractometer with CuKα radiation, operated at 40 kV and 30 mA, while data were collected at 2θ between 10° and 90°, with a step size of 0.04° and a collection time of 1 s/step. Scanning electron microscope (SEM, JSM-6330F) was used to obtain the microstructure and morphology of the prepared samples. Transmission electron microscopy (TEM) observations were conducted employing a FEI Tecnai G2 Spirit working at 120 kV. High resolution transmission electron microscopy (HRTEM) was performed in a FEI Tecnai G2 F30 electron microscope. Nitrogen adsorption/desorption isotherms were obtained at 77 K with a Micromeritics ASAP 2020 system. Brunauer–Emmett–Teller (BET) surface area was determined by a multipoint BET method using the adsorption data in the relative pressure (P/P₀) range of 0.15–0.3. Fourier-transform infrared spectroscopy (FT-IR, EQUINOX 55) was carried out at a resolution of 4 cm⁻¹, with KBr as a reference and the spectra were recorded from 4000 to 400 cm⁻¹. Raman spectra were collected using a Raman spectrometer (Nicolet NXR 9650), and X-ray photoelectron spectroscopy (XPS; ESCALab250; Mg-Ka, 15 kV, 18 mA) was conducted on an X-ray Photoelectron Spectrometer. The optical absorption property of the samples was measured using UV-vis (UV–vis) spectroscopy (Lambda 950), and the photoluminescence (PL) property were measured on an FLUOROLOG-3-TAU Steady State Fluorescence Spectrophotometer (Jobin Yvon) at room temperature.

2.4. Photocatalytic activity assessment

The photocatalytic activity of the prepared samples was evaluated by the photocatalytic degradation of gaseous styrene under the visible light irradiation in a cubic quartz reactor as described in our previous report [33]. Typically, 25 ± 1.5 ppmv of gaseous styrene with dry air at a flow rate of 20 mL min⁻¹ was continuously fed into the reactor, in which 0.10 g of prepared samples was loaded.

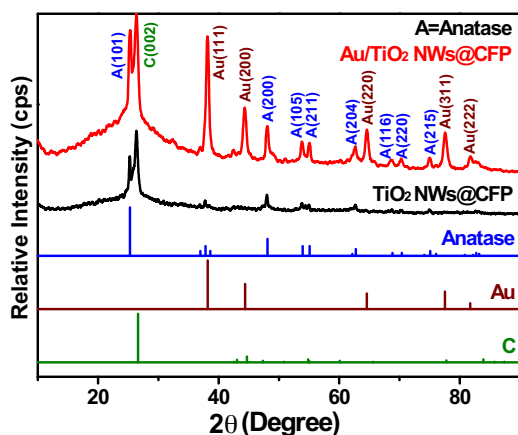**Fig 1.** XRD patterns of $TiO_2NWs@CFP$ and $Au/TiO_2NWs@CFP$ composite.

Before the lamp was switched on, the gaseous styrene was allowed to reach the adsorption equilibrium at room temperature in the dark. Then, the reactor was irradiated under a 300 W xenon lamp (CEL-HXF 300, Techcomp) with a 420 nm cut-off filter, which was fixed vertically top of the reactor with the distance of 6 cm (the light intensity was controlled at 70 mW cm^{-2} on the surface of photocatalysts). At given intervals, the gaseous samples were sampled from the reactor using a gas tight syringe (Agilent, Australia) and injected into a gas chromatography (GC-900A) equipped with a flame ionization detector for the concentration analysis. The temperatures of the column, injector and detector were 80, 200 and 230 °C, respectively.

The photocatalytic degradation efficiency of styrene was calculated according to Eq. (1).

$$\text{Degradation efficiency} = (1 - C/C_0) \times 100\% \qquad (1)$$

where C_0 and C were the concentrations of the initial and remaining styrene, respectively.

3. Results and discussion

3.1. Characterization

The XRD data of the prepared photocatalysts (Fig. 1) are used to identify the crystallographic phases of the products, along with three groups of JCPDS data including anatase TiO_2, Au and graphite. The XRD results of the obtained $TiO_2NWs@CFP$ and $Au/TiO_2NWs@CFP$ composites show that the characteristic diffraction peaks at $2\theta = 25.3°$, 48.0°, 53.9°, 55.1° and 62.7° can be attributed to the (101), (200), (105), (211) and (204) faces of anatase TiO_2 (JCPDF 21-1272) [34]. It reveals that anatase TiO_2 is the major crystallographic phase for the TiO_2 formed in the composites. Meanwhile, the peak centering at $2\theta = 26.4°$ can be indexed as (002) diffraction peak, the graphitic nature of CFP (JCPDF 41-1487) [35]. Additionally, for the $Au/TiO_2NWs@CFP$ composite, featured peaks at $2\theta = 38.2°$, 44.4°, 64.6°, 77.5° and 81.7° are indexed to (111), (200), (220), (311) and (222) crystal planes of metal Au phase (JCPDF 04-0784), indicating that metallic Au particles is formed in the resultant composite.

Further, SEM images are obtained to reveal the morphology change of CFP before and after deposition and growth of TiO_2. As Fig. 2a shows, the acid-treated CFP are 3D network structures consisting of long, straight and smooth carbon fibers with a diameter of 5–10 μm. These fibers are densely packed and randomly oriented, leading to the formation of porous and interconnected structures of CFP, which may be beneficial for the deposition of TiO_2 and the electron transport [32]. After the TiO_2 deposition onto the CFP, the

porous structure of CFP is still well retained with clearly observing the columnar contour of carbon fibers (Fig. 2b), indicating that TiO_2 structures mainly grow on the surfaces of carbon fibers and films. Comparatively, the fiber surfaces of the acid-treated CFP become rougher (Fig. 2b), indicating the successful coating of nanowires on the CFP. Further observation reveals that the entire surfaces of the carbon fibers are homogeneously encapsulated by TiO_2 NWs with the diameter of 15–30 nm and micron length (Fig. 2c and d). The close interaction between TiO_2 NWs and carbon fibers may facilitate the efficient electron collection via the CFP and suppress the recombination of electron-hole pairs during the photocatalysis [36]. In addition, a few micro-sized clusters can be found randomly dispersing around the fibers (Fig. 2e). The corresponding high-magnification image shows that these clusters are formed by the aggregation of free nanowires (Fig. 2f). All these results indicate that after hydrothermal reaction, the $TiO_2NWs@CFP$ composites are formed.

After successful preparation of the $TiO_2NWs@CFP$, the Au NPs are loaded through the photo-reduction approach to fabricate ternary composite "$Au/TiO_2NWs@CFP$". Fig. 3 shows TEM images and the Au particle size distribution of $Au/TiO_2NWs@CFP$. Clearly, Au NPs are uniformly dispersed onto the surfaces of TiO_2 NWs (Figs. 3a and b) with the mean particle size ofapproximately 1.8 nm (Fig. 3c). The corresponding HRTEM image (Fig. 3d) reveals two kinds of lattice fringes (d-spacing) of approximately 0.35 and 0.23 nm, which can be indexed as the (101) plane of anatase TiO_2 and the (111) plane of face-centered cubic Au, respectively. As such, the $Au/TiO_2NWs@CFP$ ternary composite was successfully fabricated as the following three steps: wet coating, hydrothermal reaction and photo-reduction.

Further, more structural information are obtained from FT-IR and Raman spectra. The FT-IR pattern of $Au/TiO_2NWs@CFP$ is in Fig. S1 shows the peaks at 3400 and 1650, 1587, 907 and 500 cm^{-1} which are assigned to the stretching and bending vibration of O—H band [37], C=C of the carbon fibers [38], and Ti—O, O—Ti—O [39] and Ti = O for TiO_2 [40], suggesting that carbon and titania exist in the composite. The loading of Au shows negligible effect to the molecular structure and chemical bond of $Au/TiO_2NWs@CFP$. Elemental species such as metal Au cannot be detected by FT-IR [41].

Raman spectroscopy technique is also carried out to confirm the chemical composition of $Au/TiO_2NWs@CFP$ composites (Fig. S2). Two peaks at 1356 and 1583 cm^{-1} are attributed to the D- and G-bands of graphene, respectively [42]. The D-band at around 1356 cm^{-1} can be assigned to the disordered graphitic carbon induced by sp^3 hybridization, and the G-band at around 1583 cm^{-1} indicates the presence of ordered sp^2 hybridization [43]. The peak at 142 cm^{-1} attributed to the main E_g anatase vibration mode and at 197, 395, 515, and 638 cm^{-1} assigned to the E_g, B_{1g}, A_{1g} (B_{1g}), and E_g modes of the anatase phase can be observed [44], indicating that the anatase crystallites are the major TiO_2 species, which is consistent with the XRD results. Pure metals such as Au also do not exhibit Raman scattering [45].

Since the FT-IR and Raman spectra cannot provide relative information of Au particles in the composite, XPS measurement therefore is used to characterize the valance states and the chemical environment of atoms onto the surface of prepared photocatalysts. Fig. 4a shows the XPS survey spectrum of the $Au/TiO_2NWs@CFP$ composite and the results reveal that the main elements on the prepared composite surface are Ti, O, C and Au. Figs. 4b–e show the XPS spectra of Ti 2p, O 1s, C 1s and Au 4f measured at a high resolution, respectively. As Fig. 4b shows, the peaks located at binding energies of 465.50 and 459.85 eV are designated to the Ti $2p_{1/2}$ and Ti $2p_{3/2}$ spin–orbital splitting photoelectrons in the Ti^{4+} oxidation state, respectively, slightly shifting toward higher binding energy, compared with those of the pure bulk anatase [46]. This shifting can be attributed to the transfer of conduction band electron of
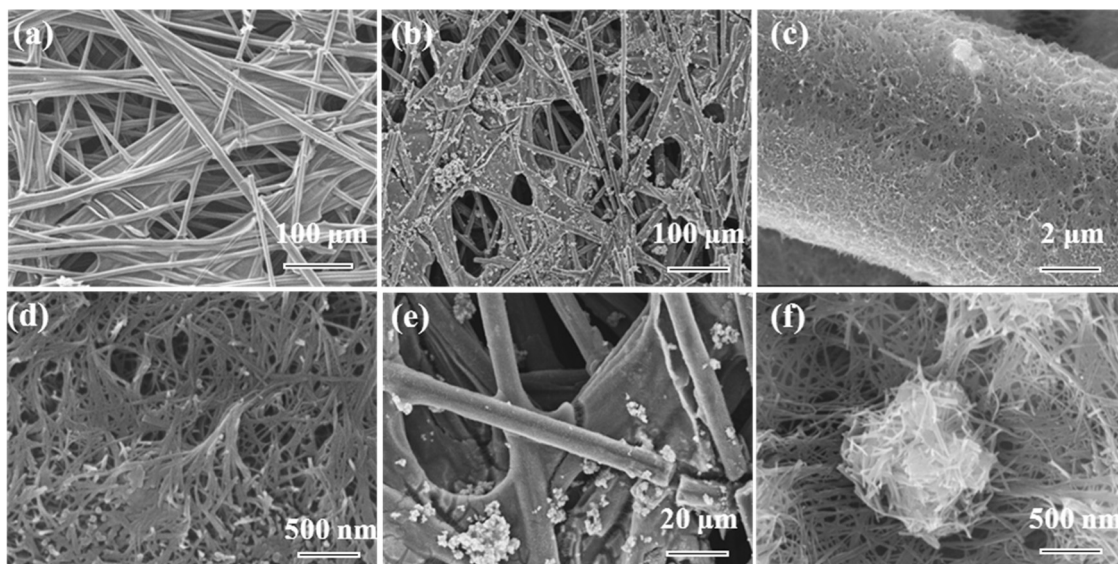
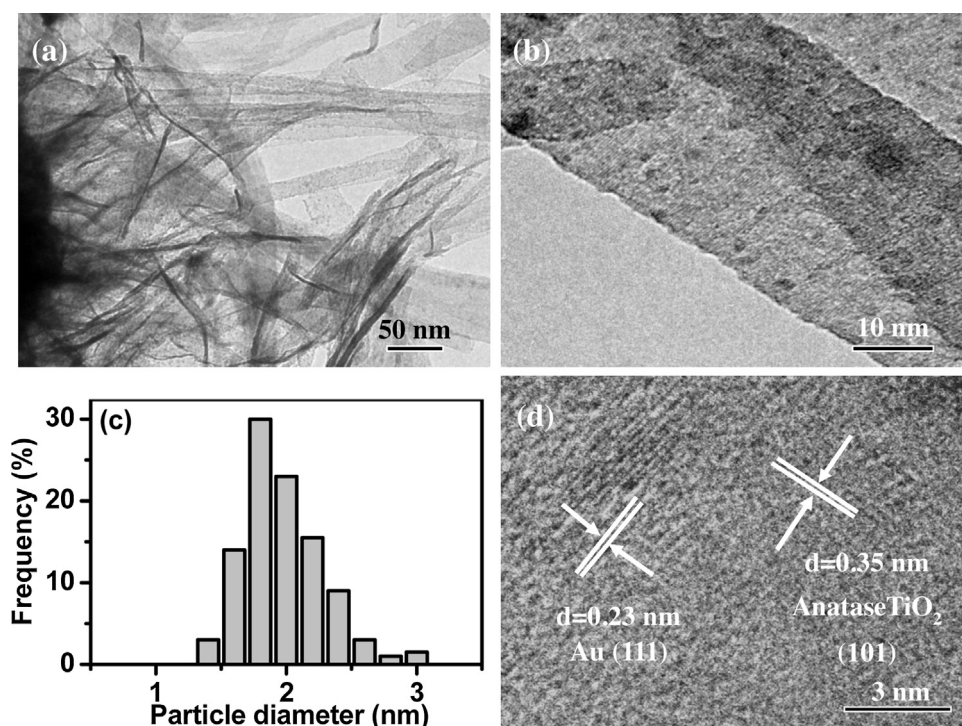**Fig. 2.** SEM images of acid-treated CFP (a) and TiO_2 NWs@CFP composite (b–f).

Fig. 3. (a,b) TEM images of Au/TiO_2NWs@CFP, (c) particle size distribution of Au NPs in and (d) HRTEM image of Au/TiO_2NWs@CFP composite.

TiO_2 to the CFP and/or Au particles [47,48]. The spin-orbital splitting between Ti $2p_{3/2}$ and Ti $2p_{1/2}$ (5.65 eV) is accordance with the chemical state of Ti^{4+} in the anatase TiO_2. The O 1 s spectrum (Fig. 4c) displays two peaks at 531.2 and 532.6 eV, which are ascribed to lattice oxygen of TiO_2 and surface-adsorbed oxygen species (such as H_2O and surface hydroxyls), respectively. The high resolution XPS spectrum of C 1 s (Fig. 4d) can be fitted to two peaks. The major peak with the binding energy of 284.8 eV is attributed to graphitic carbon (C=C bond) and C—C bond from CFP. The peak at the binding energies of 285.9 eV is assigned to the C—OH functional group. The peaks of Au $4f_{7/2}$ and Au $4f_{5/2}$ are located at 84.2 and 87.9 eV respectively, with the splitting of 3.7 eV (Fig. 4e), indicating loading metallic Au on TiO_2. XPS is further employed to calculate the content of Au, which resulted in the Au(0) percentage of 0.51%. More importantly, a shift of 0.2 eV to lower binding energy is observed by comparing with the binding energy of bulk metallic gold (84.0 and 87.7 eV), ascribing to the surface charging of Au NPs, which is due to a strong metal-support interaction [49]. Overall, the XPS results confirm the existence of interaction among Au, TiO_2 and carbon, which may improve charge separation and electron transport on the catalyst surface. This can be further confirmed by the following UV–vis and PL characterization.

UV–vis spectra of TiO_2 NWs, Au/TiO_2 NWs, TiO_2NWs@CFP and Au/TiO_2NWs@CFP are shown in Fig. 5a. All the samples exhibit strong absorption at $\lambda < 400$ nm, which is due to the electron promotion from the valence band to the conduction band of TiO_2 [34].
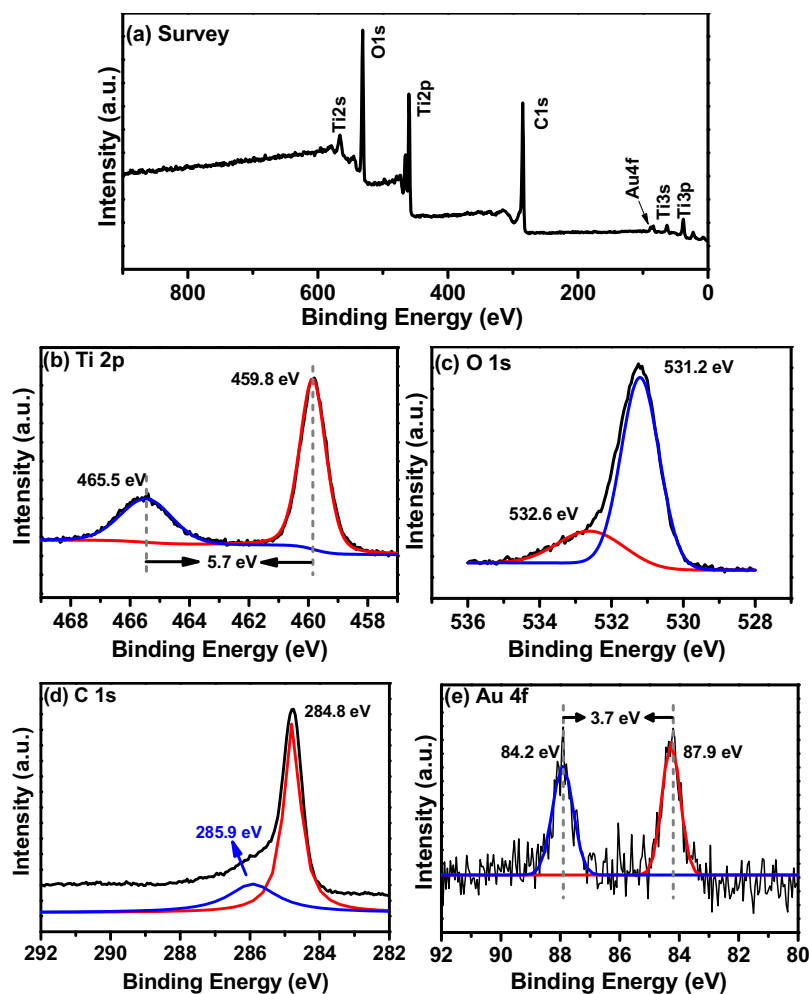
Fig. 4. XPS spectra of the Au/TiO$_2$NWs@CFP composite. (a) survey; (b) Ti 2p; (c) O 1s; (d) C 1s and (e) Au 4f.
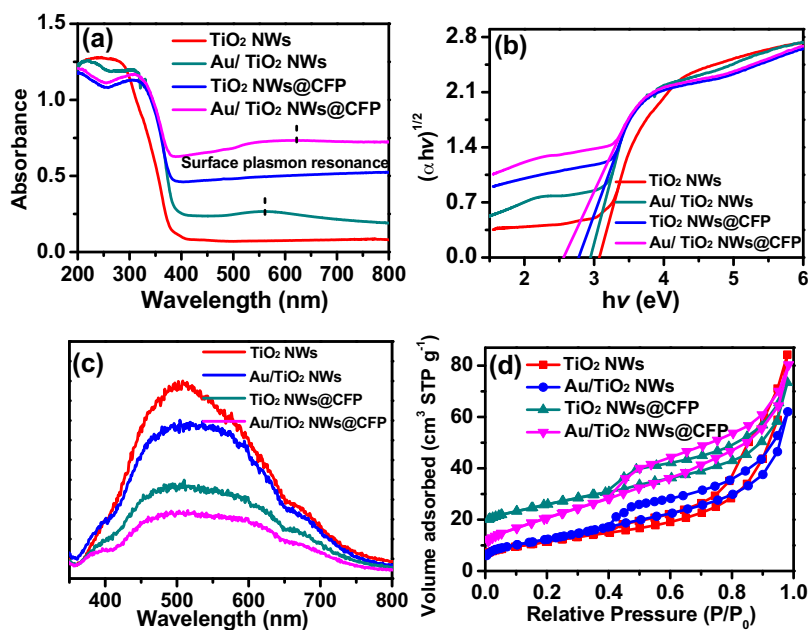

Fig. 5. (a) UV–vis diffuse reflectance spectra of prepared samples and (b) the plot of transformed Kubelka-Munk function versus the energy of light; (c) Photoluminescence (PL) spectra and (d) Nitrogen adsorption–desorption isotherm curves of TiO$_2$ NWs, TiO$_2$NWs@CFP, Au/TiO$_2$ NWs and Au/TiO$_2$NWs@CFP composite.
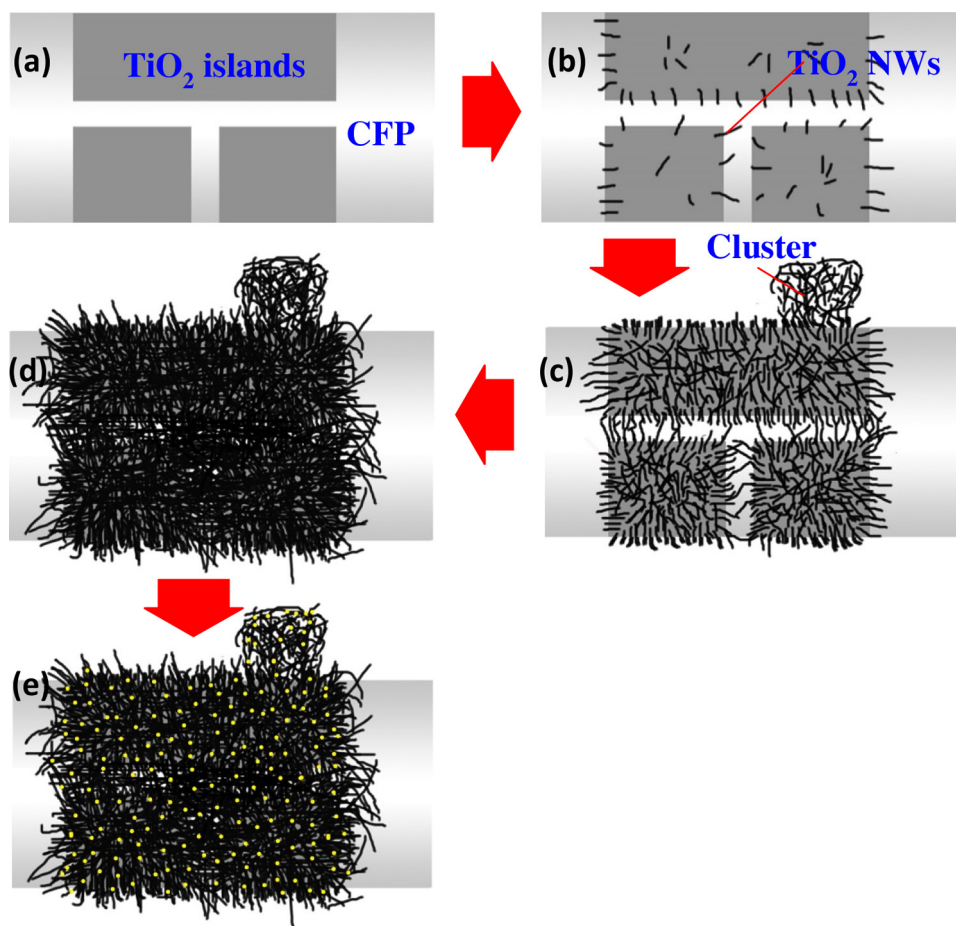
Fig. 6. Illustration of the formation process of Au/TiO$_2$ NWs@CFP composite. (a) formation of TiO$_2$ islands; (b) appearance of NWs; (c) TiO$_2$ NWs aggregate and intersect; (d) the surface of CFP is fully encapsulated by NWs and the gaps among islands disappear and the CFP surface is full of NWs and (e) loading of Au nanoparticles onto TiO$_2$ NWs@CFP through the photoreduction.

Compared to TiO$_2$ NWs, the TiO$_2$NWs@CFP composite can cause an obvious red shift of UV–vis spectra, indicating the band-gap narrowing of TiO$_2$. It can be confirmed by estimating the band gap of samples according to the plot in Fig. 5b, which is obtained via the transformation based on the Kubelka-Munk function as a function of light energy. The estimated band gap value of TiO$_2$NWs@CFP composite is approximately 2.78 eV, clearly showing a band gap narrowing as compared to the estimated 3.07 eV of the TiO$_2$ NWs. In addition, the presence of CFP in the composite leads to a wide background absorption band in the range of 400–800 nm with respect to the TiO$_2$ NWs. This can be attributed to the black nature of CFP, which can reduce the reflection of light [50]. For the Au/TiO$_2$ NWs and Au/TiO$_2$NWs@CFP composites, the light absorption in UV region is similar to that of TiO$_2$NWs@CFP composite (Fig. 5a). However, a typical wide absorption peak ranged from 500 to 700 nm (indicated by dashed lines) can be observed for the Au-loading composite, which can be ascribed to the surface plasmon resonance (SPR) response of metal Au nanoparticles [51]. The SPR can dramatically amplify the absorption of visible light and provide more photogenerated charges for the photocatalytic reactions, leading to the activity improvement of the semiconductor photocatalysts [10]. According to the Kubelka-Munk model, the estimated band gaps of Au/TiO$_2$ NWs and Au/TiO$_2$NWs@CFP are 2.94 and 2.56 eV, respectively. The narrowing of the band gaps suggests a strong interaction among CFP, Au metal and TiO$_2$ semiconductor. Moreover, the band gaps of catalysts decrease in the order TiO$_2$ NWs> Au/TiO$_2$ NWs> TiO$_2$NWs@CFP> Au/TiO$_2$NWs@CFP, indicat-

ing that Au/TiO$_2$NWs@CFP composite could be excited to produce more photogenerated charges under visible light irradiation, which may result in higher photocatalytic activity [52].

Photoluminescence emission spectrum has been widely used to investigate the fate of photogenerated electrons and holes in a semiconductor [53]. To study the effects of CFP structure and Au particles on the electron-hole recombination of TiO$_2$, PL spectra are used and the relative results are shown in Fig. 5c. TiO$_2$ NWs shows a broad emission band and the emission band corresponding to the peak position of approximately 520 nm is for anatase TiO$_2$ [54]. Comparatively, the TiO$_2$NWs@CFP and Au/TiO$_2$ NWs show the diminished PL intensities, indicating reduced charge recombination ability of electron-hole pairs under light irradiation [55]. This is because either carbonaceous species or Au particles bound to TiO$_2$ can receive the photogenerated electrons easily to efficiently inhibit the recombination of photogenerated electron-hole pairs [56]. Interestingly, the intensity of PL spectrum further decreases with the introduction of both Au particles and CFP into anatase TiO$_2$ materials. More effective charge separation on the surface of photocatalysts means more photogenerated electrons and holes can participate in the photocatalytic reaction, indicating the highest photocatalytic activity of the Au/TiO$_2$NWs@CFP ternary composite.

Fig. 5d shows the nitrogen adsorption-desorption isotherms of TiO$_2$ NWs, TiO$_2$NWs@CFP, Au/TiO$_2$ NWs and Au/TiO$_2$NWs@CFP. All the adsorption isotherms can be classified as type IV with a hysteresis loop in the IUPAC classification, indicating the presence of capillary condensation in the mesoporous structures [57,58]. These
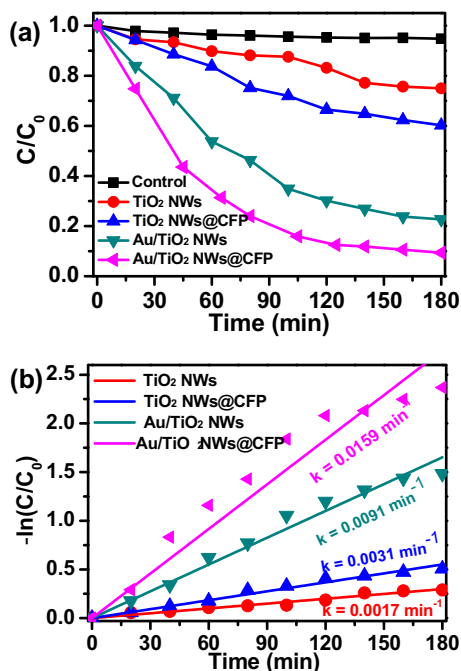
Fig. 7. (a) Photolysis of styrene as a function of irradiation time; (b) Photocatalytic degradation kinetics of TiO_2 NWs, TiO_2NWs@CFP, Au/TiO_2 NWs and Au/TiO_2NWs@CFP under visible light irradiation.

isotherms exhibit typical H3 hysteresis loops associated with the presence of slit-like pores. The pore-size distribution of TiO_2 NWs centers at 2.7 nm (Fig. S3). Similarly, the pore size distributions of Au/TiO_2 NWs, TiO_2NWs@CFP and Au/TiO_2NWs@CFP are centered at near 3.0 nm. The surface areas are 46.67, 41.67, 81.26, and 78.51 m^2/g for TiO_2 NWs, Au/TiO_2 NWs, TiO_2NWs@CFP and Au/TiO_2NWs@CFP, respectively. Obviously, the incorporation of CFP can increase the surface areas and improve the adsorptive capacity of photocatalysts, favoring for the following photocatalytic reactions [59].

3.2. Formation mechanism of Au/TiO_2NWs@CFP ternary composite

According to the above results, to obtain Au/TiO_2NWs@CFP, three main steps are needed: coating TiO_2 islands on the CFP surfaces, growth of TiO_2 NWs and deposition of Au NPs onto TiO_2 NWs. The SEM images of the Au/TiO_2NWs@CFP obtained from 110 °C hydrothermal reactions at different reaction time are shown in Fig. S4 and the corresponding formation mechanism is illustrated in Fig. 6. Firstly, the acid-treated CFP is treated with five repeated cycles of TBT-ethanol wet-coating and drying processes, resulting in the formation of innumerable micro-sized "TiO_2 islands" on the carbon fibers called "bulk TiO_2@CFP" (Figs. S4a, S4b and Fig. 6a). Then, the "bulk TiO_2@CFP" undergoes the hydrothermal reaction in the presence of mixed NaOH aqueous solution and P25 powder. After 1 h reaction, the surface of TiO_2 islands becomes rough with the appearance of some short nanowires (Fig. S4c and Fig. 6b). It should be noted that no nanowires can be formed directly onto the surface of carbon fibers when CFP was hydrothermally treated in the P25-NaOH mixture, indicating that the TiO_2 islands are the starting position of nanowires growth. Therefore, the prefabrication of bulk TiO_2@CFP seems to be a key step for the successful formation of TiO_2 NWs@CFP in this study. With the prolongation of the reaction, TiO_2 nanowires become denser and longer (Fig. S4d) and a few clusters are also formed through the aggregation of free nanowires. Further prolonging the reac-
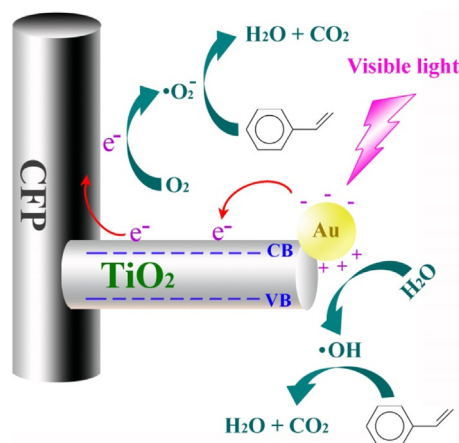

Fig. 8. Proposed mechanism for the photocatalytic degradation of styrene over Au/TiO_2NWs@CFP composite under visible light irradiation.

tion to 5 and 6 h, the gaps between the neighboring TiO_2 islands are almost filled by the continuous growing nanowires (Figs. S4e, S4f and Fig. 6c). Finally, all of the gaps disappear and CFP surfaces are fully encapsulated by TiO_2 NWs with further extending the reaction to 48 h (Figs. 2c and 6d). Clearly, the formation of the TiO_2 NWs@CFP composite undergoes the following two key steps: formation of TiO_2 islands on the CFP and in-situ growth of TiO_2 NWs. After the TiO_2 NWs growth on the CFP, the Au loading onto TiO_2NWs@CFP is carried out through photoreduction (Figs. 3a and 6e).

3.3. Photocatalytic activity evaluation

To evaluate the photocatalytic activity of the fabricated samples, the degradation of gaseous styrene was examined under visible light irradiation. As Fig. 7a shows, the photolytic degradation of styrene only under visible light irradiation is negligible. The TiO_2 NWs exhibit low activity and only 25% of styrene was removed within 3 h. This is due to the large energy gap (3.08 eV) and poor visible light absorption of TiO_2 NWs. Comparatively, TiO_2NWs@CFP displays enhanced photocatalytic activity with degradation efficiency of approximately 40% within 3 h. The enhancement could be attributed to the increased adsorption capacity to organics and electron transfer ability due to the incorporation of CFP. For the Au/TiO_2 NWs, higher photocatalytic activity was also achieved with the degradation efficiency toward styrene of approximately 73% within 3 h. The improved photocatalytic performance may be attributed to the efficient harvest of visible light by Au NPs owing to their SPR property [60] and facilitation of charge separation on the Au NPs [60,61], which can be verified by UV–vis and PL results.

As expected, Au/TiO_2NWs@CFP shows the highest photocatalytic activity and 91% of styrene is removed within 3 h. Moreover, the reaction rate constant (0.0159 min^{-1}) of Au/TiO_2NWs@CF is 9.36, 5.13, and 1.75 times higher than that of TiO_2 NWs (0.0017 min^{-1}), TiO_2NWs@CFP (0.0031 min^{-1}) and Au/TiO_2 NWs (0.0091 min^{-1}), respectively (Fig. 7b). Furthermore, Au/TiO_2NWs@CFP maintains a high degradation efficiency of *ca.* 90% after 4 recycles, suggesting high photocatalytic stability of the ternary photocatalyst (Fig. S5).

Clearly, the co-existed CFP and Au NPs in the catalyst have a synergistic effect to improve the photoactivity and photostability of the ternary composite photocatalyst. The mechanism for the enhanced photocatalytic performance is proposed in Fig. 8. Firstly, Au NPs can absorb photons under visible light irradiation because of their strong surface plasmon resonance, as indicated in the UV–vis diffuse reflectance spectra (Figs. 5a and b). As such, the introduction of

Au NPs into composite can extend the spectral response of catalyst to visible light region and improve the visible light absorption capability. Secondly, the photogenerated electrons would transfer from excited Au particles to the conduction band of TiO_2 nanowires, leaving positive holes on the Au surfaces. The CFP structures have the ability of electron capture since they exhibit high electron storage capacity and electrical conductivity. Due to lower Fermi level of CFP structures than that of TiO_2, electron transfer from TiO_2 towards the CFP surface can be prompted. The above two processes can minimize the chance of charge recombination (Fig. 5c), which improves the efficiency of charge separation and the photocatalytic activity. Moreover, the interaction among the carbon, TiO_2 and Au results in the shift of Ti and Au peaks in XPS spectra (Fig. 4), indicating that the three components form a joint electronic system and therefore facilitate the rapid transfer of photoelectrons, accelerate the separation from photoinduced holes and improve quantum efficiency for the composite system [62]. Thirdly, high specific surface area (Fig. 5d) and strong adsorption ability of CFP increase the contact opportunities of organic molecules with composite surfaces. The hierarchically porous CFP structures (Fig. 2a) can also adsorb reacting species such as O_2, H_2O and organic molecules on the catalyst surfaces. O_2 and H_2O can react with e^- and h^+ respectively, leading to the formation of various ROSs [1,63]. These radicals possess the potential to oxidize the adsorbed organics on the catalyst surfaces.

4. Conclusions

A novel photocatalyst, Au/TiO_2NWs@CFP ternary composite was fabricated using a sequent approach of wet-coating, hydrothermal reaction and photodeposition. Various characterizations showed that the CFP structures were fully covered by TiO_2 NWs, on which the Au NPs with size of ~1.8 nm were uniformly dispersed to form a unique "core-shell" structure. Ascribed to the high adsorptive capacity toward organics and capture ability of photogenerated electrons of CFP, and the excellent visible-light absorption of Au NPs with SPR, the prepared Au/TiO_2NWs@CFP ternary composite displayed the highest photocatalytic activity and stability toward gaseous styrene degradation. This study would provide a versatile strategy for the fabrication of efficient visible light activated photocatalysts for the application of atmospheric environment purification.

Acknowledgments

Appendix A. Supplementary data

Supplementary data associated with this article can be found, in the online version, at http://dx.doi.org/10.1016/j.cattod.2016.06.026.

References

[1] T.C. An, L. Sun, G.Y. Li, Y.P. Gao, G.G. Ying, Appl. Catal. B: Environ. 102 (2011) 140–146.
[2] C.L. Bianchi, S. Gatto, C. Pirola, A. Naldoni, A. Di Michele, G. Cerrato, V. Crocella, V. Capucci, Appl. Catal. B: Environ. 146 (2014) 123–130.
[3] A. Di Paola, E. Garcia-Lopez, G. Marci, L. Palmisano, J. Hazard. Mater. 211–212 (2012) 3–29.
[4] R. Zhang, A.A. Elzatahry, S.S. Al-Deyab, D. Zhao, Nano Today 7 (2012) 344–366.
[5] X. Wang, R.A. Caruso, J. Mater. Chem. 21 (2011) 20–28.
[6] K.A. Connelly, H. Idriss, Green Chem. 14 (2012) 260–280.
[7] H. Tada, T. Soejima, S. Ito, H. Kobayashi, J. Am. Chem. Soc. 126 (2004) 15952–15953.
[8] H. Li, Z. Bian, J. Zhu, Y. Huo, H. Li, Y. Lu, J. Am. Chem. Soc. 129 (2007) 4538–4539.
[9] A. Tanaka, K. Hashimoto, H. Kominami, J. Am. Chem. Soc. 134 (2012) 14526–14533.
[10] G. Wang, X. Wang, J. Liu, X. Sun, Chem. Eur. J. 18 (2012) 5361–5366.
[11] X. Huang, S. Neretina, M.A. El-Sayed, Adv. Mater. 21 (2009) 4880–4910.
[12] B. Wiley, Y. Sun, Y. Xia, Accounts Chem. Res. 40 (2007) 1067–1076.
[13] Y. Wen, B. Liu, W. Zeng, Y. Wang, Nanoscale 5 (2013) 9739–9746.
[14] D. Ali, G.M. Hosein, World Appl. Sci. J. 19 (2012) 874–879.
[15] H. Yuzawa, T. Yoshida, H. Yoshida, Appl.Catal. B: Environ. 115–116 (2012) 294–302.
[16] D. Eder, Chem. Rev. 110 (2010) 1348–1385.
[17] H.X. Shi, J.Y. Chen, G.Y. Li, X. Nie, H.J. Zhao, P.K. Wong, T.C. An, ACS Appl. Mater. Interfaces 5 (2013) 6959–6967.
[18] J.Y. Chen, H.Y. Luo, H.X. Shi, G.Y. Li, T.C. An, Appl.Catal. A: Gen. 485 (2014) 188–195.
[19] H.X. Shi, G.Y. Li, H.W. Sun, T.C. An, H.J. Zhao, P.K. Wong, Appl. Catal. B: Environ. 158–159 (2014) 301–307.
[20] B. Gao, G.Z. Chen, G. Li Puma, Appl.Catal. B: Environ. 89 (2009) 503–509.
[21] W. Wang, P. Serp, P. Kalck, J.L. Faria, J. Mol. Catal. A: Chem. 235 (2005) 194–199.
[22] Y. Ou, J. Lin, S. Fang, D. Liao, Chem. Phys. Lett. 429 (2006) 199–203.
[23] A. Kongkanand, P.V. Kamat, ACS Nano 1 (2007) 13–21.
[24] P. Zhang, C. Shao, Z. Zhang, M. Zhang, J. Mu, Z. Guo, Y. Sun, Y. Liu, J. Mater. Chem. 21 (2011) 17746–17753.
[25] S. Shanmugam, A. Gedanken, Small 3 (2007) 1189–1193.
[26] H. Wang, S. Dong, Y. Chang, J.L. Faria, J. Hazard. Mater. 235–236 (2012) 230–236.
[27] Y. Tang, S. Luo, Y. Teng, C. Liu, X. Xu, X. Zhang, L. Chen, J. Hazard. Mater. 241–242 (2012) 323–330.
[28] N. Hammer, I. Kvande, X. Xu, V. Gunnarsson, B. Tøtdal, D. Chen, M. Rønning, Catal. Today 123 (2007) 245–256.
[29] L.F. Velasco, B. Tsyntsarski, B. Petrova, T. Budinova, N. Petrov, J.B. Parra, C.O. Ania, J. Hazard. Mater. 184 (2010) 843–848.
[30] W. Wang, J. Yu, Q. Xiang, B. Cheng, Appl. Catal. B: Environ. 119–120 (2012) 109–116.
[31] T.Y. Ma, J. Ran, S. Dai, M. Jaroniec, S.Z. Qiao, Angew. Chem. Int. Ed. 54 (2015) 4646–4650.
[32] T. Tao, L. Zhang, H. Jiang, C. Li, J. Nanomater 2014 (2014) 568561.
[33] T.C. An, J.Y. Chen, X. Nie, G.Y. Li, H.M. Zhang, X.L. Liu, H.J. Zhao, ACS Appl. Mater. Interfaces 4 (2012) 5988–5996.
[34] N. Zhang, S. Liu, X. Fu, Y.-J. Xu, J. Phys. Chem. C 115 (2011) 9136–9145.
[35] B.K. Vijayan, N.M. Dimitrijevic, D. Finkelstein-Shapiro, J. Wu, K.A. Gray, ACS Catal. 2 (2012) 223–229.
[36] J.Y. Chen, G.Y. Li, Y. Huang, H.M. Zhang, H.J. Zhao, T.C. An, Appl. Catal. B Environ. 123–124 (2012) 69–77.
[37] J. Steyn, G. Pattrick, M.S. Scurrell, D. Hildebrandt, M.C. Raphulu, E. van der Lingen, Catal. Today 122 (2007) 254–259.
[38] K.M. Metz, P.E. Colavita, K.Y. Tse, R.J. Hamers, J. Power Sources 198 (2012) 393–401.
[39] P.R. Liu, Y. Wang, H.M. Zhang, T.C. An, H.G. Yang, Z.Y. Tang, W.P. Cai, H.J. Zhao, Small 8 (2012) 3664–3673.
[40] Y. Masuda, T. Ohji, K. Kato, Cryst. Growth Des. 10 (2010) 913–922.
[41] Y.J. Zhu, N. Olson, T.P. Beebe, Environ. Sci. Technol. 35 (2001) 3113–3121.
[42] Y. Yang, L. Qu, L. Dai, T.S. Kang, M. Durstock, Adv. Mater. 19 (2007) 1239–1243.
[43] A.E. Daugaard, S. Hvilsted, T.S. Hansen, N.B. Larsen, Macromolecules 41 (2008) 4321–4327.
[44] W. Zhou, K. Pan, Y. Qu, F. Sun, C. Tian, Z. Ren, G. Tian, H. Fu, Chemosphere 81 (2010) 555–561.
[45] R. Baddour-Hadjean, J.-P. Pereira-Ramos, Chem. Rev. 110 (2010) 1278–1319.
[46] D. Song, J. Hrbek, R. Osgood, Nano Lett. 5 (2005) 1327–1332.
[47] T. Ioannides, X.E. Verykios, J. Catal. 161 (1996) 560–569.
[48] G. An, W. Ma, Z. Sun, Z. Liu, B. Han, S. Miao, Z. Miao, K. Ding, Carbon 45 (2007) 1795–1801.
[49] P. Fu, P. Zhang, Appl. Catal. B: Environ. 96 (2010) 176–184.
[50] L.W. Zhang, H.B. Fu, Y.F. Zhu, Adv. Funct. Mater. 18 (2008) 2180–2189.
[51] A. Kumar, S. Mandal, P.R. Selvakannan, R. Pasricha, A.B. Mandale, M. Sastry, Langmuir 19 (2003) 6277–6282.
[52] H. Wang, H.L. Wang, W.F. Jiang, Chemosphere 75 (2009) 1105–1111.
[53] J.G. Yu, H.G. Yu, B. Cheng, X.J. Zhao, J.C. Yu, W.K. Ho, J. Phys. Chem. B 107 (2003) 13871–13879.
[54] K. Fujihara, S. Izumi, T. Ohno, M. Matsumura, J. Photochem. Photobiol. A Chem. 132 (2000) 99–104.
[55] H. Tang, K. Prasad, R. Sanjines, P.E. Schmid, F. Levy, J. Appl. Phys. 75 (1994) 2042–2047.
[56] C. Yu, J.C. Yu, Catal. Lett 129 (2009) 462–470.
[57] J. Liu, T. An, G. Li, N. Bao, G. Sheng, J. Fu, Microporous Mesoporous Mater. 124 (2009) 197–203.

[58] T.C. An, J.K. Liu, G.Y. Li, S.Q. Zhang, H.J. Zhao, X.Y. Zeng, G.Y. Sheng, J.M. Fu, Appl. Catal. A: Gen. 350 (2008) 237–243.

[59] B. Gao, C. Peng, G. Chen, G. Lipuma, Appl. Catal. B: Environ. 85 (2008) 17–23.

[60] C. Gomes Silva, R. Juarez, T. Marino, R. Molinari, H. Garcia, J. Am. Chem. Soc. 133 (2011) 595–602.

[61] J.M. Jung, M. Wang, E.J. Kim, C. Park, S.H. Hahn, Appl. Catal. B: Environ. 84 (2008) 389–392.

[62] L. Zhao, X. Chen, X. Wang, Y. Zhang, W. Wei, Y. Sun, M. Antonietti, M.M. Titirici, Adv. Mater. 22 (2010) 3317–3321.

[63] L. Sun, G.Y. Li, S.G. Wan, T.C. An, Chemosphere 78 (2010) 313–318.